PHYSICAL REVIEW B **90**, 085311 (2014)

All-optical NMR in semiconductors provided by resonant cooling of nuclear spins interacting with electrons in the resonant spin amplification regime

E. A. Zhukov,[1] A. Greilich,[1] D. R. Yakovlev,[1,2] K. V. Kavokin,[2,3] I. A. Yugova,[1,3] O. A. Yugov,[1,3] D. Suter,[4] G. Karczewski,[5] T. Wojtowicz,[5] J. Kossut,[5] V. V. Petrov,[3] Yu. K. Dolgikh,[3] A. Pawlis,[6] and M. Bayer[1]
[1] *Experimentelle Physik 2, Technische Universität Dortmund, 44221 Dortmund, Germany*
[2] *Ioffe Physical-Technical Institute, Russian Academy of Sciences, 194021 St. Petersburg, Russia*
[3] *Physical Faculty of Saint Petersburg State University, 198504 St. Petersburg, Russia*
[4] *Experimentelle Physik 3, Technische Universität Dortmund, 44221 Dortmund, Germany*
[5] *Institute of Physics, Polish Academy of Sciences, 02668 Warsaw, Poland*
[6] *Department Physik, Universität Paderborn, 33098 Paderborn, Germany*

(Received 24 February 2014; revised manuscript received 12 August 2014; published 25 August 2014)

Resonant cooling of different nuclear isotopes manifested in optically induced nuclear magnetic resonances (NMR) is observed in n-doped CdTe/(Cd,Mg)Te and ZnSe/(Zn,Mg)Se quantum wells and for donor-bound electrons in ZnSe:F and GaAs epilayers. By time-resolved Kerr rotation used in the regime of resonant spin amplification, we can expand the range of magnetic fields where the effect can be observed up to nuclear Larmor frequencies of 170 kHz. The mechanism of the resonant cooling of the nuclear spin system is analyzed theoretically. The developed approach allows us to model the resonant spin amplification signals with NMR features.

DOI: 10.1103/PhysRevB.90.085311 PACS number(s): 71.35.−y, 78.47.−p, 78.67.De

I. INTRODUCTION

Nuclear magnetic resonance (NMR) is a well-established technique which is widely used to analyze structures and electronic states in solids [1,2]. NMR is one of the key technologies for the implementation of quantum information processing, as the nuclear spins are almost ideal qubits for the manipulation and storage of the quantum information [3]. The realization of this potential in semiconductor nanostructures requires significant technical improvements to reach extremely high sensitivity and nanometer-scale resolution.

An important step in this direction was the optical detection of NMR (ODNMR) excited by radio-frequency (rf) fields. For this purpose, the effect of resonant changes of the nuclear polarization on the electron spin polarization can be measured through the polarization of the photoluminescence [4–9] or as Faraday and Kerr rotation [10] (for reviews see Refs. [11–13]). Being well established for bulk semiconductors, ODNMR has been successfully applied also to semiconductor quantum wells (QWs) [14–20] and quantum dots (QDs) [21] with much smaller numbers of nuclear spins contributing to the signal.

The next key achievement was the realization of the optically induced NMR or the so-called "all-optical NMR", where the dynamical nuclear polarization (DNP) was induced and detected by purely optical means. For the resonant addressing of the NMR, the rf magnetic field is replaced with the oscillating Knight field of the spin-polarized electrons [9,22,23]. The oscillating Knight field is provided by either intensity or polarization modulation of the laser light that photogenerates spin-oriented electrons in semiconductors. All-optical NMR has also been realized on the basis of the time-resolved pump-probe Faraday/Kerr rotation technique, where the coherent Larmor precession of the electron spins is detected [24–27]. NMR has been demonstrated in different magnetic fields and corresponding Larmor frequencies by using different techniques for the modulation of the laser light: mechanical choppers (1–6 kHz), photoelastic modulators (50–100 kHz), electro-optical modulators (1–10 MHz), or the repetition frequency of mode-locked lasers of typically around 80 MHz.

The all-optical NMR technique can manifest itself in two different ways: resonant heating or resonant cooling of the nuclear spin system (NSS):

(i) The resonant heating is typically observed when the sample is pumped with light of constant helicity, while the intensity of light is modulated. In this case nuclei are dynamically polarized (cooled) in the same way as under cw circularly-polarized excitation. But, since the number of photoexcited electrons is modulated, the nuclei are affected by an oscillating component of the Knight field, which, if the modulation frequency is close to resonance for a certain isotope, efficiently heats up the nuclear system, reducing polarization of nuclear spins. This experimental scheme is similar to the conventional optically detected NMR, the only difference being that the radio-frequency magnetic field is replaced with the optically modulated Knight field.

(ii) Resonant cooling is observed when pumping light with alternating helicity is used. Under these conditions, the dynamic nuclear polarization is strongly suppressed if the modulation period is shorter than the transverse relaxation time in the NSS [28]. However, if the modulation frequency matches the NMR frequency in the external magnetic field applied in the Voigt geometry, the efficiency of the DNP sharply increases resulting in the resonant cooling of the NSS. The reason for the DNP enhancement is synchronization of the Larmor precession of the injected nonequilibrium nuclear spin with the oscillating Knight field, which results in an efficient extraction of entropy from the NSS and therefore a reduction of the spin temperature. The nuclear polarization gained in this way has so far been observed via the contribution of the Overhauser field to the Hanle effect, which is the depolarization of the electron spin in the transverse magnetic field [29,30]. The signal from the resonant cooling has a typical dispersionlike shape, as distinct from the resonant heating that produces absorptionlike signals.

For semiconductor nanostructures, the all-optical NMR by means of the pump-probe Faraday/Kerr rotation has been realized on modulation-doped GaAs/(Al,Ga)As quantum wells under conditions of the resonant heating of the NSS [24–26]. We are not aware about observation of the resonant cooling of the NSS by these techniques.

The use of the Hanle effect for the NMR detection imposes limitations on the range of applicable magnetic fields and, consequently, of NMR frequencies. These limitations are especially severe for structures with long electron spin lifetimes, where Hanle curves are as narrow as a few Gauss. The corresponding NMR frequencies do not exceed 10 kHz, which is comparable with the width of the resonance lines in semiconductors and, therefore, does not allow us to resolve important details such as isotopic structure, quadrupole splitting, etc. This situation is typical for n-doped quantum wells and quantum dots. Electron spin dephasing times in these structures can be as long as 30–100 ns, which has been documented for quantum wells based on GaAs, CdTe, and ZnSe semiconductors [31–34]. It exceeds the typical repetition period of the mode-locked pulsed lasers of 13 ns and an accumulation of the electron spin coherence can be realized here. The resulting electron spin polarization can be conveniently measured in the resonant spin amplification (RSA) regime [35,36].

In this paper, we extend the all-optical NMR studied for the resonant spin amplification regime of the pump-probe Kerr rotation technique and investigate a variety of II-VI QWs and II-VI and III-V semiconductor epilayers. The chosen experimental conditions result in sharp NMR features in the RSA spectra associated with the resonant cooling of the nuclear spin system. We develop a theoretical approach to analyze the underlying mechanism, which predicts further modifications of the RSA spectra due to dynamical nuclear polarization.

The paper is organized as follows. Section II provides details of the experimental techniques and of the studied samples. Section III describes the experimental results. Section IV is devoted to quantitative theoretical considerations of the resonant nuclear spin cooling in n-doped quantum wells. Experimental results are compared with the modeling. In the conclusions, we compare our RSA technique for studying the nuclear spin system with earlier experimental techniques.

II. EXPERIMENTS

Time-resolved pump-probe Kerr rotation (TRKR) technique in the resonant spin amplification (RSA) regime [27,35,36] was used to study the interaction of electron spins with the nuclear spin system and demonstrate the resonant nuclear spin cooling. The electron spin coherence was generated by a train of circularly polarized pump pulses of 1.5-ps duration (spectral width of about 1 meV) generated by a mode-locked Ti:sapphire laser operating at a repetition frequency of 75.7 MHz (repetition period $T_R = 13.2$ ns). The pump helicity was modulated between σ^+ and σ^- polarizations by means of photoelastic modulators (PEM) operating at frequencies of $f_\mathrm{m} = 42$, 50, and 84 kHz, so that in average the samples were equally exposed to both polarizations of the pump. To alternate the circular light with 84 kHz we used the PEM in $\lambda/4$ retardation mode and set the lock-in amplifier to this frequency. In order to double the operation frequency up to 168 kHz, this PEM was used in a $\lambda/2$ retardation mode with an additional $\lambda/4$ plate placed at an angle of 45° to the linear polarization axis and the lock-in detection was set to the second harmonic.

The photon energy of the pump pulse was tuned into resonance with the negatively charged excitons (negative trions, T^-) of the studied QWs, which allows us to generate spin coherence for the resident electrons in the QWs [37,38]. To realize that in ZnSe-based QWs the pump beam was frequency doubled by a nonlinear Beta Barium Borate (BBO) crystal [32]. For the epilayers, the laser photon energy was resonant with the donor-bound exciton optical transitions. The induced electron spin coherence (either for the resident electron in QWs or for the electrons on donors) was monitored by linearly polarized probe pulses reflected from the excited area, which were time delayed with respect to the pump pulses by a mechanical delay line. The rotation angle of the polarization plane of the reflected probe beam (Kerr rotation) was measured by a balanced photodetector connected to a lock-in amplifier. The pump and probe beams had the same photon energy. For the RSA measurements, the probe-pulse arrival time was fixed at a small negative delay ($\Delta t \sim -50$ ps) prior to the pump pulse and the magnetic field was scanned across a small range close to zero. The average pump power was kept at the relatively low level of $P_\mathrm{pump} = 1$–$5\ \mathrm{W/cm^2}$, and the probe power (P_probe) was about one order of magnitude smaller than that of the pump.

The samples were placed in a vector magnet system consisting of three orthogonal superconducting split coils [39]. The measurements were performed in magnetic fields up to 3 T applied perpendicular to the structure growth axis $\mathbf{B} \perp \mathbf{z}$ and for the pump wave vector ($\mathbf{k}_\mathrm{pump}$) parallel to the z axis, i.e., in Voigt geometry. The vector magnet system allows us to compensate residual magnetic fields along other axes, which are commonly present in superconducting split-coil solenoids. The scanning rate of the magnetic field in our measurements was 1–2 mT/min. The increasing of the scanning rate by three times did not lead to changes of the shape and width of NMR features. Samples were immersed in pumped liquid helium at a temperature of $T = 1.8$ K.

For photoluminescence (PL) measurements, a continuous-wave (cw) laser with photon energy of 2.32 eV was used for the CdTe-based QWs and GaAs epilayer, and a cw laser with 3.05 eV for the ZnSe-based structures. PL signals were detected with a Si-based charged-coupled-device camera attached to a 0.5-m spectrometer.

For this study, we selected samples with sufficiently long spin dephasing times $T_s^* > 30$ ns in order to be able to measure them in the RSA regime. Quantum well structures and epilayers based on three different material systems of the II-VI and III-V semiconductors CdTe/(Cd,Mg)Te, ZnSe/(Zn,Mg)Se, ZnSe:F, and GaAs were used.

The studied CdTe/$\mathrm{Cd_{0.78}Mg_{0.22}Te}$ QW heterostructure (No. 031901C, sample No. 1) was grown by molecular-beam epitaxy on a (100)-oriented GaAs substrate followed by a 2-μm CdTe buffer layer. It has five periods, each of them consisting of a 20-nm-thick CdTe QW and a 110-nm-thick $\mathrm{Cd_{0.78}Mg_{0.22}Te}$ barrier. An additional 110-nm-thick barrier was grown on top of this layer sequence to reduce the contribution of surface charges. The barriers were modulation doped with iodine donors. Electrons from the barrier donors, being collected in the QWs, provide there a two-dimensional electron gas (2DEG) with a density of about $n_e = 1.1 \times 10^{10}$ cm^{-2}. Detailed studies of the optical properties and the carrier spin coherence in this structure were published in Refs. [31,37,40]. The g factor of the resident electrons $g_e = -1.64 \pm 0.02$ was determined from the Larmor precession frequency in magnetic fields exceeding 0.5 T.

A homogeneously fluorine-doped 100-nm-thick ZnSe epilayer was grown by molecular-beam epitaxy on (001)-oriented GaAs substrate (No. 2029, sample No. 2). The concentration of the fluorine donors is about 10^{15} cm^{-3}. The ZnSe:F layer was grown on top of a 20-nm-thick Zn$_{1-x}$Mg$_x$Se buffer layer that prevents carrier diffusion into the GaAs substrate. The magnesium concentration of this layer was kept below 15% to maintain good crystal quality. The optical properties of this sample and information on the electron spin coherence can be found in Ref. [41]. The g factor for the donor-bound electrons is 1.13 ± 0.02.

A 20-nm-thick ZnSe/Zn$_{1-x}$Mg$_x$Se single QW was grown by molecular-beam epitaxy on a (001)-oriented GaAs substrate (No. 2018, sample No. 3). The QW is surrounded by Zn$_{1-x}$Mg$_x$Se barrier layers with thicknesses of 24 and 30 nm. The magnesium concentration of these layers was kept below 15%. This structure was nominally undoped, but due to residual impurities and charge redistribution to surface states, the QW at low temperatures contains resident electrons with density not exceeding 10^{10} cm^{-2}. The g factor for the resident electrons in the QW is 1.13 ± 0.02.

The studied GaAs epilayer was grown by molecular-beam epitaxy on a (001)-oriented semi-insulating GaAs substrate (sample No. 4). The epilayer was nominally undoped, but contains residual donors with concentration of about 10^{16} cm^{-3} and $g_e = -0.44 \pm 0.02$.

III. EXPERIMENTAL RESULTS

A. CdTe-based QW

Figure 1(a) shows the photoluminescence spectrum of the 20-nm-thick CdTe/(Cd,Mg)Te QW, which consists of the exciton and trion emission lines separated by the trion binding energy of 2 meV. The pump-probe Kerr rotation signal measured for this QW on the trion resonance at $B = 0.25$ T is shown in Fig. 2(a). The characteristic oscillations correspond to the Larmor precession of the electron spin about the external magnetic field. This signal is observed at much longer delays than the exciton or trion recombination times, which are shorter than 100 ps [37]. Therefore, it can be related to the spin coherence of resident electrons. The dephasing of this spin coherence lasts longer than the pump repetition period $T_R = 13.2$ ns. As a result, a considerable signal amplitude is observed at negative delays, i.e., prior to the pump-pulse arrival. This behavior is qualitatively similar for all samples studied in this paper. Therefore, for other samples we will show only RSA spectra.

The long dephasing time T_s^* of the electron spin coherence exceeding $T_R = 13.2$ ns allows us to perform measurements in the RSA regime. Figure 2(b) shows the RSA signals for the trion and exciton resonances with the magnetic field scanned from −7 to +7 mT. A typical RSA signal has periodically spread RSA peaks. The peak distance on the magnetic field scale corresponds to one period of the electron

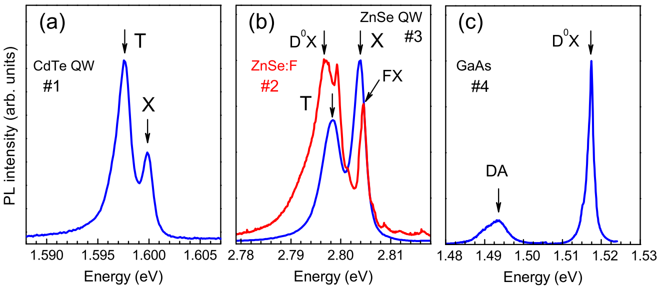

FIG. 1. (Color online) Photoluminescence spectra of studied structures: (a) 20-nm-thick CdTe/(Cd,Mg)Te QW; (b) ZnSe:F epilayer and 20-nm-thick ZnSe/(Zn,Mg)Se QW; (c) GaAs epilayer. Exciton (X), trion (T), donor-bound exciton D^{0}X, free exciton (FX), and donor-acceptor recombination (DA) lines are marked by arrows. $B = 0$ T and $T = 1.8$ K.

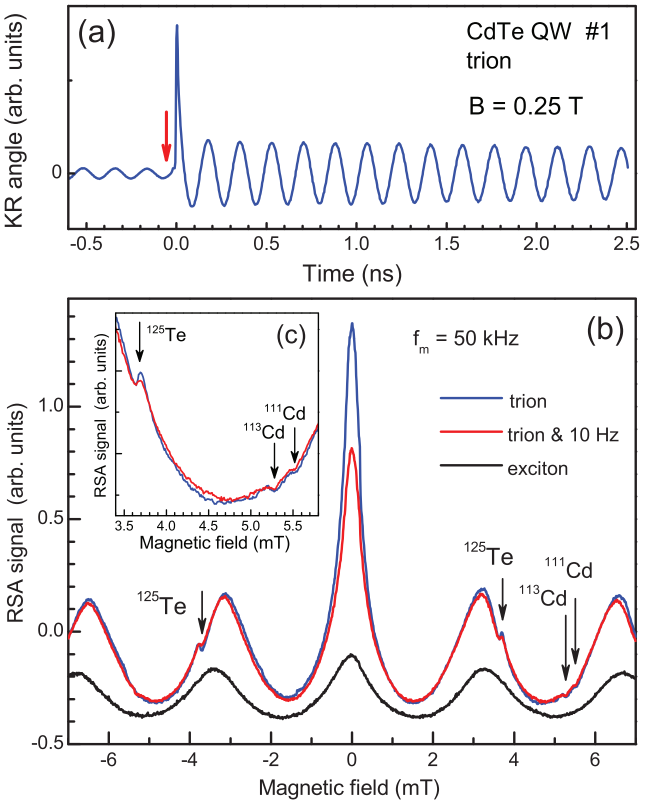

FIG. 2. (Color online) (a) Kerr rotation pump-probe signal of 20-nm-thick CdTe/(Cd,Mg)Te QW measured at trion resonance. $B = 0.25$ T and $T = 1.8$ K. Red arrow shows the time delay of $\Delta t = -80$ ps at which the RSA signals were detected. (b) RSA signals measured at the trion (blue line) and exciton (black line) resonances for $f_{\rm m} = 50$ kHz. The red line shows the trion signal measured with an additional amplitude modulation of the pump beam at 10 Hz. $P_{\rm pump} = 1$ W/cm^2 and $P_{\rm probe} = 0.2$ W/cm^2. Inset (c) zooms the NMR features. Calculated $B_{\rm NMR}$ from Table I for different isotopes are marked by arrows.

TABLE I. Calculated values of B_{NMR} given in mT for the resonant features experimentally observed in the studied structures [42–47]. I_α is the nuclear spin and μ_α is the nuclear magnetic moment for the specific isotope α.

			Resonance magnetic field (mT)			
Isotope	I_α	μ_α	42 kHz	50 kHz	84 kHz	168 kHz
^{111}Cd	1/2	−0.5943		5.52		
^{113}Cd	1/2	−0.6217		5.28		
^{125}Te	1/2	−0.8871		3.69		
^{67}Zn	5/2	+0.8754		18.67		
^{77}Se	1/2	+0.534		6.14	10.3	20.7
^{69}Ga	3/2	+2.016	4.10			
^{71}Ga	3/2	+2.562	3.23			
^{75}As	3/2	+1.439	5.75			

Larmor precession. The width of the RSA peaks is determined by the spin dephasing time T_s^* [35,36].

The unusual feature of the RSA signals from the trion, shown by the blue curve in Fig. 2(b), is the strong intensity of the zero-field RSA peak with respect to the other peaks at finite magnetic fields. An additional amplitude modulation of the pump beam at a very low frequency of 10 Hz by a mechanical chopper resulted in suppression of the zero-field peak amplitude by 40%, as shown by the red curve. This is a strong hint that the enhancement of the zero-field RSA peak is related to the polarization of the nuclear spin system and a feedback of the nuclei on the electron spin polarization measured by RSA. The enhancement is almost absent for the RSA signals measured on the excitons [black curve in Fig. 2(b)]. This is in line with the suggested explanation, as in the case of trion the localized resident electrons can better polarize nuclei in the volume of their localization, compared to the weaker localized electrons, whose spin coherence is induced via excitons. It was shown for CdTe/(Cd,Mg)Te QWs that resident electrons with different localization are addressed via the trion and exciton states (see Fig. 20 in Ref. [37]).

Interaction between the electron and nuclear spin systems appears also in the form of relatively weak dispersive resonance features in the RSA signals at magnetic fields of ±3.7; ±5.3 and ±5.6 mT, where the NMR features at $f_{\mathrm{m}} = 50$ kHz for ^{125}Te, ^{113}Cd, and ^{111}Cd isotopes are expected. The arrows in Fig. 2(b) show the calculated resonance magnetic fields B_{NMR} for these isotopes, the numerical values are collected in Table I. Similar NMR features were reported earlier for Hanle curves of III-V semiconductor structures being related to the resonant cooling of the NSS [23,30]. Since these experiments were performed under different experimental conditions, one needs to develop a suitable theory that can describe resonant cooling of the NSS and its detection in the RSA regime. Such a model will be suggested below.

Note that in order to observe NMR features in RSA signals a finite signal amplitude is required, i.e., the NMR features are very weak and hardly observable between RSA peaks, where the signal amplitude has a minimum. To make them more pronounced, one can either vary the modulation frequency f_{m} to shift B_{NMR} or broaden the RSA peaks by shortening the dephasing time, e.g., by means of increasing the pump power.

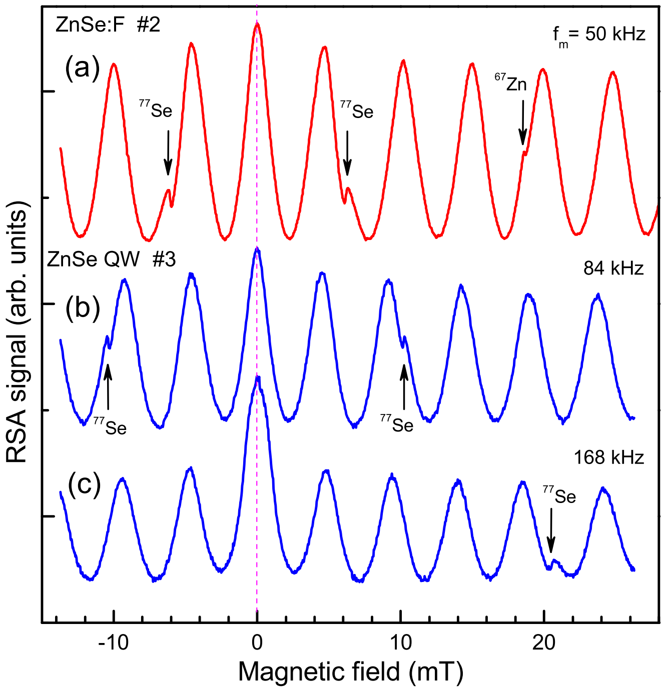

FIG. 3. (Color online) RSA signals for ZnSe:F epilayer (a) and 20-nm-thick ZnSe/(Zn,Mg)Se QW (b), (c) measured for different modulation frequencies at $T = 1.8$ K. $\Delta t = -35$ ps, $P_{\mathrm{pump}} = 5$ W/cm^2, and $P_{\mathrm{probe}} = 0.2$ W/cm^2. Calculated B_{NMR} from Table I are shown by arrows.

B. ZnSe:F epilayer and ZnSe-based QW

Photoluminescence spectra of the ZnSe:F epilayer and ZnSe/(Zn,Mg)Se QW are shown in Fig. 1(b). The epilayer spectrum consists of several lines (for details see Ref. [41]), two of them relevant to this study are marked by arrows. They are the donor-bound exciton (D^{0}X) at 2.7970 eV and free exciton with heavy hole (FX) at 2.8045 eV. The binding energy of the exciton to the fluorine donor is about 7.5 meV. The QW spectrum has two lines at 2.7984 and 2.8030 eV corresponding to the trion and exciton recombinations, respectively, in the ZnSe QW. They are separated by 4.6 meV, which is the binding energy of the negatively charged trion.

Examples for the pump-probe Kerr rotation signals in the ZnSe:F epilayers and ZnSe-based QWs can be found in Refs. [32,41]. The RSA signals for these samples, measured for various modulation frequencies are shown in Fig. 3. As one can see, the RSA spectra of the epilayer and QW are very similar to each other. Pronounced NMR features for the ^{77}Se and ^{67}Zn isotopes are clearly seen. They are shifted to higher magnetic fields with increasing modulation frequency from 50 up to 168 kHz. For $f_{\mathrm{m}} = 50$ kHz resonances are seen at ±6.2 (^{77}Se) and +18.6 mT (^{67}Zn), for $f_{\mathrm{m}} = 84$ kHz at ±10.2 mT (^{77}Se), and for $f_{\mathrm{m}} = 168$ kHz at +20.5 mT (^{77}Se).

C. GaAs epilayer

The photoluminescence spectrum of the GaAs epilayer (sample No. 4) is shown in Fig. 1(c). It contains two lines at 1.5174 and 1.4932 eV corresponding to the donor-bound exciton (D^{0}X) and donor-acceptor recombination (DA),

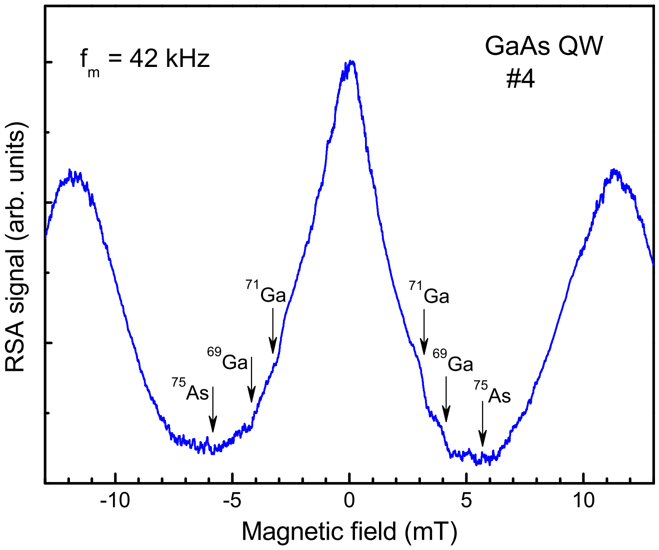

FIG. 4. (Color online) RSA signal for GaAs epilayer measured at resonant pumping of the D^{0}X transition at $f_{\mathrm{m}} = 42$ kHz. $T = 1.8$ K. $\Delta t = -50$ ps, $P_{\mathrm{pump}} = 5$ W/cm^2, and $P_{\mathrm{probe}} = 0.2$ W/cm^2. Calculated B_{NMR} from Table I are shown by arrows.

respectively [42]. The RSA signal measured with resonant pumping of the D^{0}X transition is shown in Fig. 4. The in-plane electron g factor of $g_e = -0.44$ has been evaluated. NMR features for the ^{71}Ga, ^{69}Ga, and ^{75}As isotopes are seen at negative and positive magnetic fields of ± 3.2, ± 4.1, and ± 5.8 mT. These fields match well the expected NMR features for $f_{\mathrm{m}} = 42$ kHz, compared with the calculated values in Table I.

IV. THEORY

It has been shown in the experiment that the NMR features became very pronounced in the RSA spectra under conditions, in which on the first view no mean spin from the electrons should be transferred into the NSS: (i) high symmetry of the structures with zinc-blende crystal lattice grown along the (001) axis; (ii) the pump beam is parallel to the structure growth axis $\mathbf{k}_{\mathrm{pump}} \parallel \mathbf{z}$; (iii) the external magnetic field is perpendicular to the structure growth axis $\mathbf{B} \perp \mathbf{z}$ and $\mathbf{B} \perp \mathbf{k}_{\mathrm{pump}}$; (iv) the structure is equally exposed by σ^+ and σ^- circularly polarized pump. To disclose the responsible mechanisms, a detailed theoretical analysis is needed, which is given in this section. In Sec. IV A, we consider the main idea of the cooling of the nuclear spin system by optically oriented electron spins in the RSA regime. Then, in Sec. IV B, we describe calculations of the RSA spectra in detail. In the first approximation, we model an electron spin dynamics in external magnetic fields and calculate an accumulated electron spin polarization after train of pulses (Secs. IV B 1–IV B 4). At the end of Sec. IV B 4 we obtain the average electron spin, which changes the nuclear spin polarization. This allows us to calculate hyperfine field. Finally, in Sec. IV B 5 we model the RSA spectra with accounting of the nuclear contributions by obtaining the accumulated electron spin in external magnetic fields with the addition of the hyperfine nuclear field.

A. Cooling of the nuclear spin system via interaction with spin-polarized electrons

As mentioned in the Introduction, the resonant cooling of the NSS in exact Voigt geometry is the result of synchronization of the spin injection into the NSS, the oscillatory magnetic field applied to the NSS (this can be the Knight field of the electrons), and the Larmor precession of nuclear spins in the static transverse magnetic field. In the case of RSA experiments, this picture becomes more complicated since pulsed excitation brings in high-frequency components of the mean electron spin, which are essential for the overall spin dynamics, as their superposition forms the observed series of RSA peaks. Here, we extend and develop the theory of resonant cooling [12] to adopt it to this new experimental design.

The resonant cooling of the NSS can be theoretically described using modified Provotorov equations for two effective temperatures describing the dipole-dipole and Zeeman nuclear spin reservoirs [12,48]. In order to calculate the average nuclear field and its effect upon the mean electron spin (which we optically probe in RSA experiments), a more intuitive, though quite rigorous, approach can be used, which invokes the rotating-frame approximation [12,23] (see also Chap. 2 in Ref. [1]).

Under the conditions of RSA, DNP in the rotating frame has certain specifics because of the presence of "slow" and "fast" oscillating components of the electron spin. Oscillation of the slow component with an angular frequency $\omega_{\mathrm{m}} = 2\pi f_{\mathrm{m}} = (2.64 \div 10.55)\times 10^5$ rad/s is provided by the PEM with $f_{\mathrm{m}} = 42 \div 168$ kHz, while the fast component is due to electron spin Larmor precession. Under RSA conditions, the main contributions to the fast component are made by oscillations with frequencies commensurate with the repetition rate of the pulsed laser of 75.7 MHz. At the magnetic field corresponding to the maximum of the first RSA peak, the corresponding Larmor frequency is $\omega_L = 2\pi/T_{\mathrm{R}} = 4.75\times 10^8$ rad/s $= 2\pi \times 75.7$ MHz. We will show in the following that the slow component of the electron spin polarization is responsible for the DNP, while the resultant nuclear field is detected by its effect on the fast components of the electron spin polarization.

We now consider the electron spin polarization photogenerated by the pump pulses and averaged over many pulses and Larmor periods, as it evolves as a function of the phase of the PEM. The average spin polarization, $\mathbf{S}$ is perpendicular to the external magnetic field $\mathbf{B}$ and oscillates with the angular frequency ω_{m} of the PEM. Its oscillation can be represented as a superposition of two vectors:

$$\mathbf{S}(t) = \mathbf{S}_{+}(t) + \mathbf{S}_{-}(t). \qquad (1)$$

Here, $\mathbf{S}_{+}(t)$ and $\mathbf{S}_{-}(t)$ are also perpendicular to $\mathbf{B}$ and rotate clockwise and counterclockwise, respectively. Each of these mean spin vectors produces a double effect on the NSS: (i) spin relaxation of electrons by nuclei creates a spin flow into the NSS, and (ii) the nuclear spins become subjected to a rotating Knight field. If we turn to the rotating frame, where $\mathbf{S}_{+}$ (or $\mathbf{S}_{-}$) is static, then $\mathbf{S}_{-}$ (or, correspondingly, $\mathbf{S}_{+}$) rotates at double frequency $2\omega_{\mathrm{m}} \gg T_{2,N}^{-1}$ and its contribution to DNP can be neglected. Here, $T_{2,N}$ is the transverse spin relaxation time of the nuclei. Under these conditions, the averaged

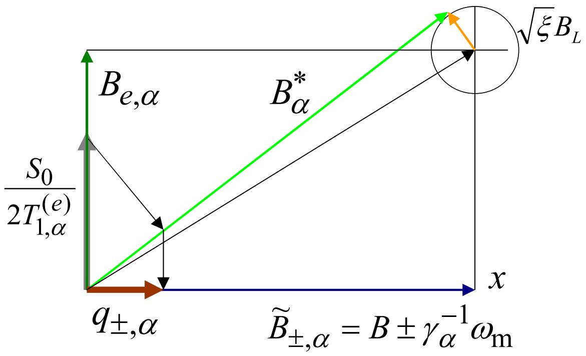

FIG. 5. (Color online) Scheme of the electron-nuclear spin interaction process in the rotating coordinate system.

(over the rotation period) spin flow **q** is parallel to **B** and equals the sum of the contributions from $\mathbf{S}_+$ and $\mathbf{S}_-$ ($\mathbf{q}_+$ and $\mathbf{q}_-$), which can be calculated independently in the frame where the corresponding spin component is static:

$$q = q_+ + q_- = \frac{S_0}{2}\sum_\alpha \frac{1}{T^{(e)}_{1,\alpha}}\left[\frac{B_{e,\alpha}\tilde{B}_{+,\alpha}}{(\tilde{B}_{+,\alpha})^2 + (B_{e,\alpha})^2 + \xi B_L^2} + \frac{B_{e,\alpha}\tilde{B}_{-,\alpha}}{(\tilde{B}_{-,\alpha})^2 + (B_{e,\alpha})^2 + \xi B_L^2}\right]. \qquad (2)$$

Here, S_0 is the averaged electron spin, $T^{(e)}_{1,\alpha}$ is the longitudinal spin relaxation time of the nuclei due to their interaction with electrons, $\tilde{B}_{\pm,\alpha} = B \pm \gamma_\alpha^{-1}\omega_{\rm m}$ (the term $\pm\gamma_\alpha^{-1}\omega_{\rm m}$ along B occurs at the transition to the rotating frame), γ_α is the gyromagnetic ratio of the αth isotope, $B_{e,\alpha} = b_{e,\alpha}S_0/2$ is the Knight field, $b_{e,\alpha} = -2A_\alpha/(N\hbar\gamma_\alpha)$, N is the number of nuclei in the localization volume of the electron wave function, A_α is the hyperfine constant for the isotope α, B_L is the rms local field due to the nuclear dipole-dipole interaction, and ξ is a dimensionless parameter of the order of one, accounting for electron spin correlation [12]. We refer the reader to Ref. [12] for a detailed theory of nuclear spin cooling in the Knight field leading to Eq. (2).

The electron-nuclear spin interaction processes are shown schematically in Fig. 5 in the rotating frame. The hyperfine-induced flip-flop transitions of the electron and any isotope group α of the nuclear spins create nonequilibrium nuclear spin polarization parallel to the component of the mean spin of the electrons, which is static in the rotating frame, with the rate $S_0/(2T^{(e)}_{1,\alpha})$ (see Fig. 5). Because of the nuclear spin precession in constant ($B_{e,\alpha}$ and $\tilde{B}_{\pm,\alpha}$) and random ($\sqrt{\xi}B_L$) magnetic fields, only the nuclear spin projection on the total field B^*_α (in the rotating frame) survives. The time-averaged spin flow q_+ (or q_-) in the laboratory frame is then obtained by projecting the spin flow in the rotating frame on the direction of $\tilde{B}_{\pm,\alpha}$, which coincides with B. This double projecting brings about the fraction containing various magnetic fields in Eq. (2), which is just a product of the two cosines arising in the projection procedure. The value of ξ cannot be obtained from this simple geometric model and requires a microscopic calculation within the spin-temperature formalism [12,49,50].

The general rate equation for the nuclear spin projection on the external field [see Eq. (11.13) in Ref. [11]] reads as

$$\langle\dot{I}_\alpha\rangle = q_\alpha - \frac{1}{T^{(e)}_{1,\alpha}}\left(\frac{\langle I_\alpha\rangle}{Q_\alpha} + \langle S_T\rangle\right) - \frac{\langle I_\alpha\rangle}{T_{N,\alpha}}, \qquad (3)$$

where Q_α is the coefficient which shows an efficiency of nuclear spin polarization by electrons. In frame of spin density matrix theory [51] assuming absence of correlations in the nuclear spin system $Q_\alpha = \frac{I_\alpha(I_\alpha+1)}{s(s+1)}$, s and I_α are the electron spin and nuclear spin for isotope α. $\langle S_T\rangle$ is the equilibrium value of the electron spin, corresponding to the thermal population of its Zeeman sublevels, and $T_{N,\alpha}$ is the relaxation time of nuclear spin by all mechanisms other than interaction with electrons. Assuming that $\langle S_T\rangle \ll S_0$ and $T_{N,\alpha} \gg T^{(e)}_{1,\alpha}$, we obtain for the steady-state regime

$$\langle I_\alpha\rangle = Q_\alpha T^{(e)}_{1,\alpha} q_\alpha = \frac{Q_\alpha S_0}{2}\left[\frac{B_{e,\alpha}\tilde{B}_{+,\alpha}}{(\tilde{B}_{+,\alpha})^2 + (B_{e,\alpha})^2 + \xi B_L^2} + \frac{B_{e,\alpha}\tilde{B}_{-,\alpha}}{(\tilde{B}_{-,\alpha})^2 + (B_{e,\alpha})^2 + \xi B_L^2}\right]. \qquad (4)$$

The hyperfine field created by the mean nuclear spin acting on the electron spins is [28]

$$B_N = \sum_\alpha b_{N,\alpha}\langle I_\alpha\rangle = \sum_\alpha \frac{A_\alpha \varkappa_\alpha}{\mu_B g_e}\langle I_\alpha\rangle, \qquad (5)$$

where $b_{N,\alpha} = A_\alpha\varkappa_\alpha/(\mu_B g_e)$, $\varkappa_\alpha$ is the abundance of isotopes α. The field $\mathbf{B}_N$ adds to the external field $\mathbf{B}$ ($\mathbf{B}_N$ is almost collinear with $\mathbf{B}$) and modifies the precession frequency of the electron spin $\omega_L = g_e\mu_B(B + B_N)/\hbar$ in the RSA regime. One can see that the dependence of the mean nuclear spin on the external magnetic field [Eq. (4)] and, therefore, the dependence of the hyperfine field created by the α isotopes $B_{N,\alpha}$ [Eq. (5)] has two derivativelike features (resonances) around, $B = \pm\omega_{\rm m}/\gamma_\alpha$. The widths of these resonances are equal to $\sqrt{(B_{e,\alpha})^2 + \xi B_L^2}$ and the phases are determined by $b_{N,\alpha}$. Indeed, A_α is proportional to the nuclear magnetic moment $\mu_\alpha = \hbar\gamma_\alpha$, and, therefore, the Knight field $B_{e,\alpha} = b_{e,\alpha}\frac{S_0}{2} = -\frac{A_\alpha}{\mu_\alpha}\frac{S_0}{N}$ does not depend on the value and sign of μ_α. It follows then from Eq. (4) that the mean nuclear spin gained by resonant cooling is not sensitive to the sign of μ_α either. Therefore, the sign of the nuclear field at certain detunings of the external field from the resonance, according to Eq. (5), is determined by the signs of the electron g factor and the magnetic moment μ_α of the resonant isotope. For instance, the resonances in GaAs and CdTe, both having negative electron g factors, will look inverted with respect to each other because the magnetic isotopes of Cd and Te have negative hyperfine constants, while for all the nuclear species in GaAs, the hyperfine constants are positive (see Table II). In CdTe and ZnSe the resonances have the same shape because opposite signs of their electronic g-factors are compensated by the opposite signs of the hyperfine constants.

TABLE II. Parameters of nuclear isotopes with nonzero spin in the studied structures. All data for nuclear spins I_α and magnetic momenta μ_α are taken from Ref. [52]. A_α is the hyperfine constant, which is taken for a unit cell with two nuclei and $\eta_\alpha = |u_c(\boldsymbol{R}_\alpha)|^2 v_0$, where $u_c(\boldsymbol{R}_\alpha)$ is the electron Bloch function at the αth nucleus and v_0 is the unit-cell volume [43].

Species	I_α	μ_α	Abundance $\varkappa_\alpha$	η_α ($\times 10^3$)	A_α (μeV)
^{111}Cd	1/2	−0.5943	0.128	3.6[a]	−37.4
^{113}Cd	1/2	−0.6217	0.123	3.6[a]	−39.1
^{125}Te	1/2	−0.8871	0.079		−45[b]
^{67}Zn	5/2	+0.8754	0.041		3.7[c]
^{77}Se	1/2	+0.534	0.0758	3.6	33.6[d]
^{69}Ga	3/2	+2.016	0.604	2.61[e]	38.2
^{71}Ga	3/2	+2.562	0.396	2.61[e]	48.5
^{75}As	3/2	+1.439	1	4.42[e]	46

[a] From Ref. [46].
[b] From Ref. [53].
[c] From Ref. [41].
[d] From Ref. [43].
[e] From Ref. [47].

B. NMR in RSA spectra

In the RSA spectra, the electron spin polarization is measured via the Kerr rotation. Information on the nuclear spin polarization and NMR can be also obtained from the RSA spectra when the nuclei modify the electron spin polarization. To model nuclear effects in RSA spectra, we use a two-step procedure. In the first step, we neglect B_N because this field is weak in the resonant-cooling regime and calculate the electron spin polarization (and therefore the Knight field) under light excitation with alternated helicity in the external magnetic field. For these calculations, we need to account for (i) the periodic change of the pump polarization (caused by the PEM); (ii) the generation of electron spin polarization by the short pump pulse; (iii) the electron spin dynamics in the magnetic field; and (iv) the accumulation of the electron spin polarization after a train of pump pulses. This would allow us to calculate the hyperfine field, which develops as a result of resonant cooling in the sum of the external magnetic field and the Knight field. In the second step, we calculate the electron spin polarization, taking into account the nuclear field, and model the resulting RSA spectra.

1. *Polarization of the pump pulses*

One of the main features of the RSA technique is the periodic generation of the electron spin coherence by a train of laser pulses. In our experiments, the repetition period of the laser pulses is $T_R = 13.2$ ns (the pump-pulse repetition frequency is 75.7 MHz). The polarization of the pump pulses is changed periodically by the PEM with a frequency $f_{\rm m} = 42 \div 168$ kHz.

We model the excitation with light of alternating helicity in the following way. Let the pump beam before the PEM be polarized linearly along the x axis: $\boldsymbol{E}(\boldsymbol{r},t) = E_x(\boldsymbol{r},t)\boldsymbol{o}_x + \text{c.c.}$, here $E_x \sim e^{-i\omega t}$, ω is the optical frequency, and $\boldsymbol{o}_x$ is the unit vector along $\mathbf{x}$. The electric vector of the light after the PEM can be written as

$$\boldsymbol{E}(\boldsymbol{r},t) = \frac{E_x(\boldsymbol{r},t)}{\sqrt{2}}\left\{\cos\left[\frac{\phi}{2}\sin(\omega_{\rm m}t) - \frac{\pi}{4}\right]\boldsymbol{o}_+ + \sin\left[\frac{\phi}{2}\sin(\omega_{\rm m}t) - \frac{\pi}{4}\right]\boldsymbol{o}_-\right\} + \text{c.c.}, \tag{6}$$

where $\boldsymbol{o}_\pm$ are the circularly polarized unit vectors that are related to the unit vectors $\boldsymbol{o}_x \parallel \mathbf{x}$ and $\boldsymbol{o}_y \parallel \mathbf{y}$ through $\boldsymbol{o}_\pm = (\boldsymbol{o}_x \pm \mathrm{i}\boldsymbol{o}_y)/\sqrt{2}$. ϕ is the maximal phase delay created by PEM. In our Kerr rotation experiments $\phi = \pi/2$, when we use the first harmonic. One can expand Eq. (6) into a harmonic series:

$$\begin{aligned}\boldsymbol{E}(\boldsymbol{r},t) = \frac{E_x(\boldsymbol{r},t)}{2}\Bigg\{&\Bigg[-J_0\left(\frac{\pi}{4}\right) + 2\sum_{k=0}^{\infty}\left[J_{2k}\left(\frac{\pi}{4}\right)\cos(2k\omega_{\rm m}t) + J_{2k+1}\left(\frac{\pi}{4}\right)\sin\left((2k+1)\omega_{\rm m}t\right)\right]\Bigg]\boldsymbol{o}_+ \\ &+\Bigg[J_0\left(\frac{\pi}{4}\right) - 2\sum_{k=0}^{\infty}\left[J_{2k}\left(\frac{\pi}{4}\right)\cos(2k\omega_{\rm m}t) - J_{2k+1}\left(\frac{\pi}{4}\right)\sin\left((2k+1)\omega_{\rm m}t\right)\right]\Bigg]\boldsymbol{o}_-\Bigg\} + \text{c.c.},\end{aligned} \tag{7}$$

where J_k are Bessel functions.

Choosing $\phi = \pi/2$ and neglecting all terms that oscillate at higher harmonic frequencies $(2\omega_{\rm m},\ 3\omega_{\rm m},\ldots)$ we can approximately rewrite Eq. (7) as

$$\begin{aligned}\boldsymbol{E}(\boldsymbol{r},t) &= \frac{E_x(\boldsymbol{r},t)}{2}\left\{\left[2J_1\left(\frac{\pi}{4}\right)\sin(\omega_{\rm m}t) - J_0\left(\frac{\pi}{4}\right)\right]\boldsymbol{o}_+ + \left[2J_1\left(\frac{\pi}{4}\right)\sin(\omega_{\rm m}t) + J_0\left(\frac{\pi}{4}\right)\right]\boldsymbol{o}_-\right\} + \text{c.c.} \\ &\equiv E_{\sigma^+}(\boldsymbol{r},t)\boldsymbol{o}_+ + E_{\sigma^-}(\boldsymbol{r},t)\boldsymbol{o}_- + \text{c.c.}\end{aligned} \tag{8}$$

The modulation of the light by the PEM generates elliptically polarized light that changes from σ^+ to σ^- going through linear polarization.

2. *Generation of electron spin polarization*

Our consideration of the generation of the spin polarization for the resident electrons in QWs and the electrons bound to donors in bulk semiconductors is based on the approach developed in Refs. [34,36,54]. We assume that the long-lived spin polarization of the electrons is generated by resonant excitation of the negatively charged excitons (trions). Following, we consider the case of trions in QWs, while the approach is equally valid for the resonant excitation of the donor-bound excitons in bulk semiconductors. The resonant excitation of the electron spin system by a short elliptically polarized pulse can be described as

$$S_z^a = \frac{Q_+^2 - Q_-^2}{4} + \frac{Q_+^2 + Q_-^2}{2} S_z^b,$$
$$S_y^a = Q_+ Q_- S_y^b, \quad S_x^a = Q_+ Q_- S_x^b. \tag{9}$$

Here, S_z, S_y, S_x are electron spin components, and the subscripts a and b denote the spin components at a time just after or shortly before the pump-pulse arrival. In the magnetic field $\mathbf{B}||\mathbf{x}$, the S_x component does not change and we disregard it in the following. Q_+ and Q_- are associated with the powers of the σ^+ and σ^- components of the incident light. They are defined by the corresponding pulse areas $\Theta_\pm$: $Q_\pm = \cos(|\Theta_\pm|/2)$, $\Theta_\pm = \int 2\langle d\rangle E_{\sigma^\pm}(t)dt/\hbar$. Here, $\langle d\rangle$ is the dipole transition matrix element and $E_{\sigma^\pm}(t)$ are smooth envelopes of the circular components of the electric field of the laser pulse.

It follows from Eq. (8) that $E_{\sigma^\pm}(t) = E_x(\mathbf{r},t)[J_1(\frac{\pi}{4})\sin(\omega_{\mathrm{m}} t) \mp J_0(\frac{\pi}{4})/2]$ and $\Theta_\pm \approx \Theta_0[J_1(\frac{\pi}{4})\sin(\omega_{\mathrm{m}} t) \mp J_0(\frac{\pi}{4})/2]$, where $\Theta_0 = \int \langle d\rangle E_x(t)dt/\hbar$. In the low-pump-power regime ($|\Theta_0|^2 \ll 1$), which is valid for QWs [34], Eq. (9) gives us

$$S_z^a \approx \frac{|\Theta_0|^2}{16} J_0\left(\frac{\pi}{4}\right) J_1\left(\frac{\pi}{4}\right)\sin(\omega_{\mathrm{m}} t) + S_z^b, \quad S_y^a \approx S_y^b. \tag{10}$$

3. *Spin dynamics in a magnetic field*

Since the time scales of the electron and nuclear spin dynamics differ by several orders of magnitude, the fast dynamics of the single electron spin in the interval between pump pulses occurs in the sum of the external magnetic field and the frozen effective field of the nuclear spins $\mathbf{B} + \mathbf{B}_N$:

$$\mathbf{S}(t) = \{\mathbf{n}(\mathbf{n}\cdot\mathbf{S}^a) + [\mathbf{S}^a - \mathbf{n}(\mathbf{n}\cdot\mathbf{S}^a)]\cos(\omega_L t)$$
$$+ [\mathbf{S}^a - \mathbf{n}(\mathbf{n}\cdot\mathbf{S}^a)] \times \mathbf{n}\sin(\omega_L t)\}\exp(-t/T_s), \tag{11}$$

where $\mathbf{n} = (\mathbf{B} + \mathbf{B}_N)/|\mathbf{B} + \mathbf{B}_N|$ is the unit vector along the total magnetic field. It is obvious that the second and the third terms in the right side of Eq. (11) are transverse components of the electron spin polarization, which oscillate with electron Larmor precession frequency $\omega_L = |g_e\mu_B(\mathbf{B} + \mathbf{B}_N)|/\hbar$. The first term in Eq. (11) is the longitudinal component. For simplicity, here we consider isotropic spin relaxation and, therefore, all components decay with the same spin relaxation time T_s. It is worth reminding that at the first step we neglect $\mathbf{B}_N$ for the calculation of $\mathbf{S}(t)$.

The modulation period of the pump polarization is three orders of magnitude longer than the laser repetition period T_R. This leads to accumulation of electron spin polarization after a train of pump pulses with a polarization determined by the PEM.

4. *Accumulation of electron spin polarization and Knight field*

The accumulated electron spin polarization after each repetition period $\mathbf{S}(T_R)$ [given by Eq. (11)] should be equal to the spin right before the pump-pulse arrival $\mathbf{S}^b$ [given by Eqs. (9)]. Without an effective nuclear field, the resulting electron spin polarization after each pump pulse is

$$S_z^a = -\frac{Q_+^2 - Q_-^2}{4\Delta}[K_1\cos(\omega_L T_R) - 1],$$
$$S_y^a = -\frac{Q_+^2 - Q_-^2}{4\Delta} K_1 \sin(\omega_L T_R),$$
$$\Delta = 1 - (K_1 + K_2)\cos(\omega_L T_R) + K_1 K_2, \tag{12}$$
$$K_1 = Q_+ Q_- \exp(-T_R/T_s),$$
$$K_2 = \frac{Q_+^2 + Q_-^2}{2}\exp(-T_R/T_s).$$

The experimental RSA signal is proportional to the S_z component of the accumulated polarization taken in one of the circular polarizations σ^+ or σ^- (e.g., for σ^+ polarization $\Theta_- = 0$ and, therefore, $Q_- = 1$). Modeled RSA spectra without taking into account nuclear spin effects are shown in Fig. 6 (red curves) for three material systems based on

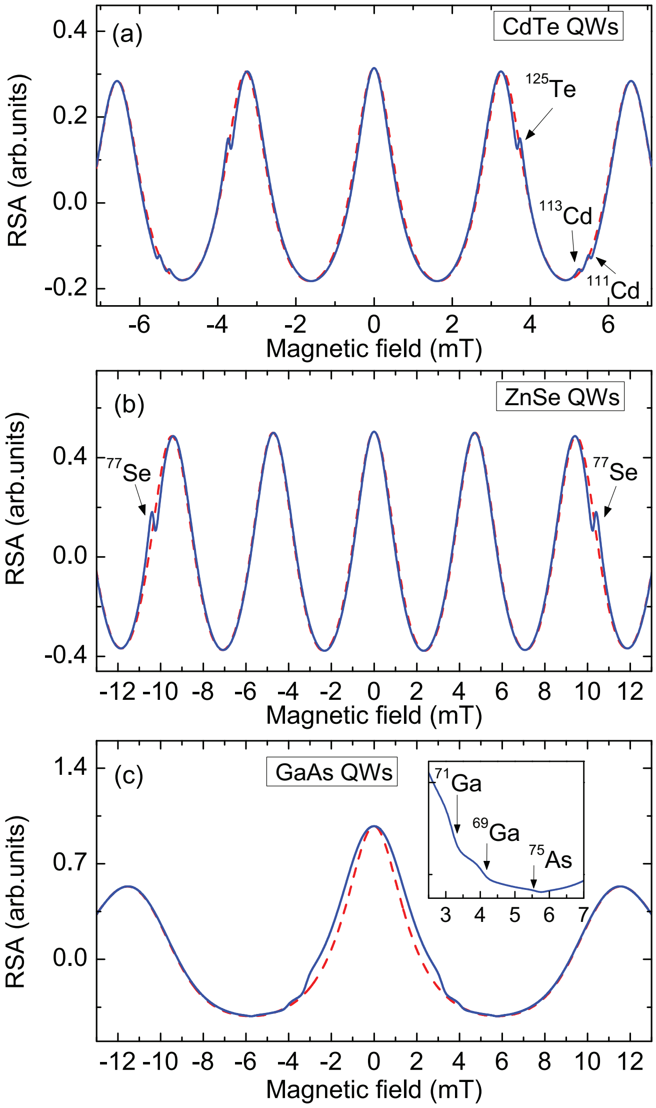

FIG. 6. (Color online) Calculated RSA spectra for CdTe-, ZnSe-, and GaAs-based QWs. Dashed (red) lines show RSA spectra without accounting for the nuclear effects. Solid (blue) lines show RSA spectra with the nuclear spin effects taken into account.

TABLE III. Parameters used for calculation of RSA spectra in Fig. 6.

QWs	CdTe	ZnSe	GaAs
g_e	−1.64	1.13	−0.44
Δg_e	0.04	0.02	0.055
b_e (mT)	−16.2 (^{111}Cd) −16.2 (^{113}Cd) −13 (^{125}Te)	−10.7 (^{67}Zn) −32.1 (^{77}Se)	−9.7 (^{69}Ga) −9.7 (^{71}Ga) −16.4 (^{75}As)
$b_{N,\alpha}$ (mT)	50.5 (^{111}Cd) 50.7 (^{113}Cd) 37.5 (^{125}Te)	2.4 (^{67}Zn) 39 (^{77}Se)	−900 (^{69}Ga) −760 (^{71}Ga) −1800 (^{75}As)
$\sqrt{\xi}B_L$ (mT)	0.012	0.006	0.3
f_m (kHz)	50	84	42
T_s(ns)	10.6	10.6	13.2

CdTe, ZnSe, and GaAs. For the electron spin ensemble, the calculated polarization is averaged over the g-factor spread with a Gaussian distribution function (see Sec. III D in Ref. [36]). The parameters used for these calculations are given in Table III. The electron spin coherence time T_s and the g-factor spread Δg_e were taken close to the experimental data.

We now turn to the calculation of the Knight field. Here, we consider again a single electron spin. Note that as the Bohr magneton μ_B is approximately 2000 times larger than the nuclear magneton, the Zeeman splitting of the electron and nuclear spin levels and their Larmor precession frequencies differ by three orders of magnitude. Therefore, the slow dynamics of the NSS is determined only by the averaged electron spin polarization. For the average of the polarization over the period from the $(m-1)$th to the mth pulse, we obtain

$$\begin{aligned}\mathbf{S}_0 &= \frac{1}{T_R}\int_{(m-1)T_R}^{mT_R}\mathbf{S}(t)dt\\ &= \mathbf{n}(\mathbf{n}\cdot\mathbf{S}^a) + \frac{\mathbf{S}^a - \mathbf{n}(\mathbf{n}\cdot\mathbf{S}^a)}{\omega_L T_R}\sin(\omega_L T_R)\\ &\quad + \frac{[\mathbf{S}^a - \mathbf{n}(\mathbf{n}\cdot\mathbf{S}^a)]\times\mathbf{n}}{\omega_L T_R}[1-\cos(\omega_L T_R)]. \qquad (13)\end{aligned}$$

Taking into account Eq. (12), we can write

$$\begin{aligned}\mathbf{S}_0 &= \sqrt{\frac{\left[\left(S_z^a\right)^2 + \left(S_y^a\right)^2\right]K_3}{(T_R/T_s)^2 + (\omega_L T_R)^2}},\\ K_3 &= \sqrt{[1 - 2\exp(-T_R/T_s)\cos(\omega_L T_R) + \exp(-2T_R/T_s)]}.\end{aligned} \qquad (14)$$

For QWs, all these equations are valid in the low-power regime described by Eq. (10) [34]. Equations (10) and (14) give us

$$\mathbf{S}_0 \approx -\frac{|\Theta_0|^2}{16}J_0\left(\frac{\pi}{4}\right)J_1\left(\frac{\pi}{4}\right)\frac{\sin(\omega_{\mathrm{m}}t)}{\sqrt{(T_R/T_s)^2 + (\omega_L T_R)^2}}. \qquad (15)$$

This is the specific expression for the oscillating electron spin polarization of Eq. (1), which results in NMR lines in the RSA spectra.

5. RSA spectra with nuclear spin effects

We use Eq. (15) for the electron field $B_e = b_e S_0/2$ to calculate from Eqs. (4) and (5) the hyperfine field B_N. Then, at the second step of our calculations, we take again Eqs. (9) and (11) and calculate the accumulated electron spin polarization in the sum of external and nuclear magnetic fields, similar to Eq. (12). The calculated polarization is again averaged over the g-factor spread with a Gaussian distribution function.

Modeled RSA spectra including the effect of the nuclear field are shown in Fig. 6 by the blue curves. The parameters for the calculations are given in Table III. b_e and $b_{N,\alpha}$ were evaluated using the A_α and μ_α values from Table II. The parameter value $\sqrt{\xi}B_L$ controlling the width of the NMR features is determined by dipole-dipole interaction [1], therefore it is proportional to $\sum_\alpha \mu_\alpha \langle r_\alpha\rangle^{-3}$, where $\langle r_\alpha\rangle$ is the average distance between nuclei. Using the known value for GaAs $\sqrt{\xi}B_L = 0.3$ mT [49], we can estimate corresponding values for CdTe (0.012 mT) and ZnSe (0.006 mT).

The number of nuclei in the localization volume of electron wave function was estimated as $16a_l^3/3a_0^3$, where a_l is the localization radius and a_0 is the lattice constant. We assumed that $a_l = 10$ nm for GaAs and for CdTe, and $a_l = 7$ nm for ZnSe.

For GaAs, good agreement was achieved with the theoretical values of $Q_\alpha = 5$. For CdTe and ZnSe, we had to take larger values of Q (three and four times larger than theoretical ones, correspondingly) to achieve good description of experimental data. This may indicate a limited validity of the existing theory [51] as applied to these materials.

Comparing the blue and red graphs in Fig. 6 one can conclude about three effects related to the electron-nuclear interaction, which become evident in the RSA spectra: (i) appearance of NMR features for different isotopes; (ii) narrowing (in CdTe and ZnSe) or broadening (in GaAs) of the zero-field RSA peak; and (iii) shift of the nonzero-field RSA peaks, which is pronounced for CdTe. One can see that the phase of the derivative shape of the NMR features in CdTe and ZnSe coincides with each other, while it is inverted in GaAs. The phase is controlled by the sign of the $b_{N,\alpha}$ field (see Table III), which either increases or decreases the equilibrium polarization of the nuclei induced by the external field. The same reason explains the changes in the linewidth of the zero-field RSA peak in the effect (ii). The shift of the nonzero RSA peaks [effect (iii)] is related to the developing of the $B_{N,x}$ component of the DNP. Its experimental appearance and theoretical description will be published elsewhere.

V. CONCLUSIONS

Our experiments and their comparison with the developed theoretical model have demonstrated the possibility to realize resonant cooling of the nuclear spin system in semiconductor nanostructures and bulk layers in the regime of resonant spin amplification (RSA). This was done by thorough adjustment of the magnetic field to the exact Voigt geometry and using a photoelastic modulator to alternate the helicity of the excitation laser at high frequency, keeping the time-averaged spin of optically oriented electrons zero within the experimental precision. Under these conditions, nuclear spin pumping is forbidden outside the resonance of the nuclear Larmor precession with the modulation frequency. All-optical NMR signals with dispersionlike shape, typical for resonant cooling, were observed when the NMR feature field was close to the position of the RSA peaks. The NMR features were detected on up to the fifth RSA peak. Thus, resonant cooling signals were observed at magnetic fields well outside the typical width of Hanle curves for the studied structures, which are nearly identical to the shape of the zero-field RSA peak [55].

As follows from the developed theory, these signals are due to cooling of the nuclei by both the z and y components of the electron mean spin. Their vector sum decays with growing transverse field B as $1/B$ rather than $1/B^2$ as does the z component usually observed in the Hanle effect. Sharp RSA peaks that rise at the magnetic fields satisfying electron spin resonance conditions at the laser repetition frequency and its overtones provide the probe for the nuclear spin polarization via its effect upon the electron spin resonance frequency and help detecting resonant cooling signals at magnetic fields well outside the width of the Hanle curve. This way, we detected all-optical NMR of all the magnetic isotopes present in the studied samples. Notably, the shape of the experimentally observed resonances are sensitive to the sign of the isotope magnetic moments, in full agreement with the theory. The difference of our findings with previously reported experiments on all-optical NMR in the RSA regime (for example, [25]) is that in our case there was no background nuclear polarization, and all observed nuclear spin effects developed exclusively at resonance fields due to resonant cooling of the nuclear spin system.

ACKNOWLEDGMENTS

The authors are thankful to I. A. Merkulov for valuable discussions. This work was supported by the Deutsche Forschungsgemeinschaft, BMBF (Project No. 05K12PE1), the Russian Ministry of Education and Science (Contract No. 11.G34.31.0067 with SPbSU and leading scientist A. V. Kavokin), and EU FET project SPANGL4Q. The authors acknowledge Saint-Petersburg State University for a research grant (No. 11.38.213.2014). The research in Poland was partially supported by the National Centre of Science (Poland) Award No. DEC-2012/06/A/ST3/00247. Growth of the ZnSe-based structures has been supported by the Deutsche Forschungsgemeinschaft (Project No. LI-668).

[1] A. Abragam, *The Principle of Nuclear Magnetism* (Oxford University Press, Oxford, 1961).
[2] R. R. Ernst, G. Bodenhausen, and A. Wokaun, *Principles of Nuclear Magnetic Resonance in One and Two Dimensions* (Oxford University Press, Oxford, 1997).
[3] M. A. Nielsen and I. L. Chang, *Quantum Computation and Quantum Information* (Cambridge University Press, New York, 2000).
[4] A. I. Ekimov and V. I. Safarov, Pis'ma Zh. Eksp. Teor. Fiz. **15**, 453 (1972) [JETP Lett. **15**, 179 (1972)].
[5] V. L. Berkovits, A. I. Ekimov, and V. I. Safarov, Zh. Eksp. Teor. Fiz. **65**, 346 (1973) [Sov. Phys.–JETP **38**, 169 (1974)].
[6] M. I. Dyakonov, V. I. Perel, V. L. Berkovits, and V. I. Safarov, Zh. Eksp. Teor. Fiz. **67**, 1912 (1974) [Sov. Phys.–JETP **40**, 950 (1975)].
[7] D. Paget, Phys. Rev. B **24**, 3776 (1981).
[8] V. K. Kalevich and V. G. Fleisher, Izv. Akad. Nauk SSSR Ser. Fiz. **47**, 2294 (1983) [Bull. Acad. Sci. USSR Phys. Ser. **47**, 5 (1983)].
[9] M. Eickhoff, B. Lenzman, G. Flinn, and D. Suter, Phys. Rev. B **65**, 125301 (2002).
[10] T. A. Kennedy, J. Whitaker, A. Shabaev, A. S. Bracker, and D. Gammon, Phys. Rev. B **74**, 161201(R) (2006).
[11] V. K. Kalevich, K. V. Kavokin, and I. A. Merkulov, in *Spin Physics in Semiconductors*, edited by M. I. Dyakonov (Springer, Berlin, 2008), pp. 309–346, Chap. 11.
[12] V. G. Fleisher and I. A. Merkulov, in *Optical Orientation*, edited by F. Meier and B. P. Zakharchenya (North-Holland, Amsterdam, 1984), pp. 173–258, Chap. 5.
[13] D. Paget and V. L. Berkovits, in *Optical Orientation*, edited by F. Meier and B. P. Zakharchenya (North-Holland, Amsterdam, 1984), pp. 381–422, Chap. 9.
[14] V. K. Kalevich, V. L. Korenev, and O. M. Fedorova, Pis'ma Zh. Eksp. Teor. Fiz. **52**, 964 (1990) [JETP Lett. **52**, 349 (1990)].
[15] G. P. Flinn, R. T. Harley, M. J. Snelling, A. C. Tropper, and T. M. Kerr, J. Luminescence **45**, 218 (1990).
[16] Marcus Eickhoff, Bjoern Lenzmann, Dieter Suter, Sophia E. Hayes, and Andreas D. Wieck, Phys. Rev. B **67**, 085308 (2003).
[17] Marcus Eickhoff and Dieter Suter, J. Magn. Reson. **166**, 69 (2004).
[18] M. Poggio and D. D. Awschalom, Appl. Phys. Lett. **86**, 182103 (2005).
[19] H. Sanada, Y. Kondo, S. Matsuzaka, K. Morita, C. Y. Hu, Y. Ohno, and H. Ohno, Phys. Rev. Lett. **96**, 067602 (2006).
[20] Y. Kondo, M. Ono, S. Matsuzaka, K. Morita, H. Sanada, Y. Ohno, and H. Ohno, Phys. Rev. Lett. **101**, 207601 (2008).
[21] D. Gammon, S. W. Brown, E. S. Snow, T. A. Kennedy, D. S. Katzer, and D. Park, Science **277**, 85 (1997).
[22] V. K. Kalevich, Fiz. Tverd. Tela **28**, 3462 (1986) [Sov. Phys.–Solid State **28**, 1947 (1986)].
[23] V. K. Kalevich, V. L. Korenev, and V. G. Fleisher, Izv. Akad. Nauk SSSR Ser. Fiz. **52**, 434 (1988) [Bull. Acad. Sci. USSR Phys. Ser. **52**, 16 (1988)].
[24] J. M. Kikkawa and D. D. Awschalom, Science **287**, 473 (2000).
[25] G. Salis, D. T. Fuchs, J. M. Kikkawa, D. D. Awschalom, Y. Ohno, and H. Ohno, Phys. Rev. Lett. **86**, 2677 (2001).
[26] G. Salis, D. D. Awschalom, Y. Ohno, and H. Ohno, Phys. Rev. B **64**, 195304 (2001).
[27] *Semiconductor Spintronics and Quantum Computation*, edited by D. D. Awschalom, D. Loss, and N. Samarth (Springer, Berlin, 2002).
[28] *Optical Orientation*, edited by F. Meier and B. P. Zakharchenya (North-Holland, Amsterdam, 1984).

[29] V. K. Kalevich, V. D. Kulkov, and V. G. Fleisher, Fiz. Tverd. Tela **22**, 1208 (1980) [Sov. Phys.–Solid State **22**, 703 (1980)].

[30] V. K. Kalevich and B. P. Zakharchenya, Fiz. Tverd. Tela **37**, 3525 (1995) [Sov. Phys.–Solid State **37**, 1938 (1995)].

[31] G. V. Astakhov, M. M. Glazov, D. R. Yakovlev, E. A. Zhukov, W. Ossau, L. W. Molenkamp, and M. Bayer, Semicond. Sci. Technol. **23**, 114001 (2008).

[32] E. A. Zhukov, D. R. Yakovlev, A. Schwan, O. A. Yugov, A. Waag, L. W. Molenkamp, and M. Bayer, Phys. Status Solidi B, doi:10.1002/pssb.201350233 (2014).

[33] M. Griesbeck, M. M. Glazov, E. Ya. Sherman, D. Schuh, W. Wegscheider, C. Schüller, and T. Korn, Phys. Rev. B **85**, 085313 (2012).

[34] I. A. Yugova, A. A. Sokolova, D. R. Yakovlev, A. Greilich, D. Reuter, A. D. Wieck, and M. Bayer, Phys. Rev. Lett. **102**, 167402 (2009).

[35] J. M. Kikkawa and D. D. Awschalom, Phys. Rev. Lett. **80**, 4313 (1998).

[36] I. A. Yugova, M. M. Glazov, D. R. Yakovlev, A. A. Sokolova, and M. Bayer, Phys. Rev. B **85**, 125304 (2012).

[37] E. A. Zhukov, D. R. Yakovlev, M. Bayer, M. M. Glazov, E. L. Ivchenko, G. Karczewski, T. Wojtowicz, and J. Kossut, Phys. Rev. B **76**, 205310 (2007).

[38] D. R. Yakovlev and M. Bayer, in *Spin Physics in Semiconductors*, edited by M. I. Dyakonov (Springer, Berlin, 2008), pp. 135–177, Chap. 6.

[39] E. A. Zhukov, O. A. Yugov, I. A. Yugova, D. R. Yakovlev, G. Karczewski, T. Wojtowicz, J. Kossut, and M. Bayer, Phys. Rev. B **86**, 245314 (2012).

[40] E. A. Zhukov, D. R. Yakovlev, M. Bayer, G. Karczewski, T. Wojtowicz, and J. Kossut, Phys. Status Solidi B **243**, 878 (2006).

[41] A. Greilich, A. Pawlis, F. Liu, O. A. Yugov, D. R. Yakovlev, K. Lischka, Y. Yamamoto, and M. Bayer, Phys. Rev. B **85**, 121303(R) (2012).

[42] H. Landoldt and R. Börnstein, *Semiconductors: II-VI Compounds; Semimagnetic Compounds* (Springer, Berlin, 1999), Vol. III.41.B.

[43] M. Syperek, D. R. Yakovlev, I. A. Yugova, J. Misiewicz, I. V. Sedova, S. V. Sorokin, A. A. Toropov, S. V. Ivanov, and M. Bayer, Phys. Rev. B **84**, 085304 (2011); **84**, 159903(E) (2011).

[44] K. M. Whitaker, S. T. Oschsebein, A. L. Smith, D. C. Echodu, B. H. Robinson, and D. R. Gamelin, J. Phys. Chem. C **114**, 14467 (2010).

[45] I. A. Merkulov, A. L. Efros, and M. Rosen, Phys. Rev. B **65**, 205309 (2002).

[46] A. Nakamura, D. Paget, C. Hermann, C. Weisbuch, and G. Lampel, Solid State Commun. **30**, 411 (1979).

[47] D. Paget, G. Lampel, B. Sapoval, and V. I. Safarov, Phys. Rev. B **15**, 5780 (1977).

[48] I. A. Merkulov and M. N. Tkachuk, Zh. Eksp. Teor. Fiz. **83**, 620 (1982) [Sov. Phys.–JETP **56**, 342 (1982)].

[49] M. I. Dyakonov and V. I. Perel, in *Optical Orientation*, edited by F. Meier and B. P. Zakharchenya (North-Holland, Amsterdam, 1984), pp. 11–72, Chap. 2.

[50] M. I. Dyakonov and V. I. Perel, Zh. Eksp. Teor. Fiz. **68**, 1514 (1975) [Sov. Phys.–JETP **41**, 759 (1975)].

[51] M. I. Dyakonov and V. I. Perel, Zh. Eksp. Teor. Fiz. **65**, 362 (1973) [Sov. Phys.–JETP **38**, 177 (1974)].

[52] *American Institute of Physics Handbook*, 3rd ed., edited by Dwight E. Gray (McGraw-Hill, New York, 1972), Chap. 8b.

[53] C. Testelin, F. Bernardot, B. Eble, and M. Chamarro, Phys. Rev. B **79**, 195440 (2009).

[54] E. A. Zhukov, D. R. Yakovlev, M. M. Glazov, L. Fokina, G. Karczewski, T. Wojtowicz, J. Kossut, and M. Bayer, Phys. Rev. B **81**, 235320 (2010).

[55] The zero-field RSA peak [Eq. (12)] has the same form as the standard expression for the Hanle effect [28]: the electron spin depolarization in a transversal magnetic field under continuous wave pumping. The influence of the inhomogeneous distribution of g factors on the Hanle effect is typically quite weak and, as a rule [31,36], the extracted spin dephasing time is controlled by the nuclear spin fluctuations, i.e., by T_s^*. As compared with the Hanle effect, the studies of the resonant spin amplification allow one to directly extract the magnetic field dependence of the spin dephasing time, and consequently, evaluate the spread of g factors Δg.